This article has been accepted for publication in IEEE Transactions on Medical Robotics and Bionics. This is the author's version which has not been fully edited and content may change prior to final publication. Citation information: DOI 10.1109/TMRB.2024.3464668

Selectively Tunable Joints with Variable Stiffness for a Magnetically-Steerable 6-DOF Manipulator

Simon Frieler[1], Sarthak Misra[1], Venkatasubramanian Kalpathy Venkiteswaran[1]

***Abstract*—Robotic manipulators are used across various surgical tasks, including endoscopic and laparoscopic procedures. Operating in small and constrained spaces during these procedures requires the manipulators to have high dexterity and control over the motion path but with a small footprint. In this work, we propose a modular design of a magnetically-guided small-sized robotic manipulator. The manipulator has discrete universal joints that allow ease of actuation. Variable stiffness is incorporated into the joints to allow the locking and unlocking of individual degrees of freedom (DOFs). The design is modular and allows extension to additional DOFs. The range of each DOF is 60 ° and is controlled by a pair of shape memory polymer flexures; four flexures comprise one joint. With rolling-contact elements, the design eliminates problems with buckling and pushability. A custom-designed heating element triggers the flexures to switch from a high (0.57 Nmm/°) to a low stiffness (0.06 Nmm/°) state within 14 (±0.8) s. Ambient cooling secures shape-locking within 64 (±3.7) s. In an experiment, a 6-DOF version of the manipulator navigates around obstacles in confined spaces and remains shape-locked for stable operation. Practical application is demonstrated through simulated gastroscopy and polypectomy using inserted surgical tools.**

***Index Terms*—Universal joint, variable stiffness, shape memory polymer (SMP), minimally invasive surgery (MIS), magnetic actuation.**

I. Introduction

ROBOT-ASSISTED surgery has gained popularity for reducing incision sizes, speeding up recoveries, shortening surgery durations, and lowering hospitalization costs [1]. Currently in robotic surgery, multiple ports of entry are required to access spread-out surgical sites with rigid, less maneuverable instruments. By contrast, highly maneuverable instruments have a greater workspace and can reduce the number of entry ports. Additionally, it allows clinicians to select the ports of entry more optimally, mitigating patient risks compared to rigid instruments, which demand extensive pre-planning due to their limited insertion options [2]. The rising prominence of continuum and discrete-link manipulators designed for surgical applications such as endoscopy [3], [4], neurosurgery [5], [6], and laparoscopy [7], [8] underlines the demand for robotic manipulators that are both flexible and compact to access deep-seated surgical sites.

Simon Frieler, Sarthak Misra, and Venkatasubramanian Kalpathy Venkiteswaran are with the Surgical Robotics Laboratory, Department of Biomechanical Engineering, University of Twente, 7500 AE Enschede, The Netherlands (e-mail: s.frieler@utwente.nl; v.kalpathyvenkiteswaran@utwente.nl).

Sarthak Misra is also with the Surgical Robotics Laboratory, Department of Biomaterials and Biomedical Technology, University of Groningen and University Medical Centre Groningen, 9713 GZ Groningen, The Netherlands (e-mail: s.misra@utwente.nl).

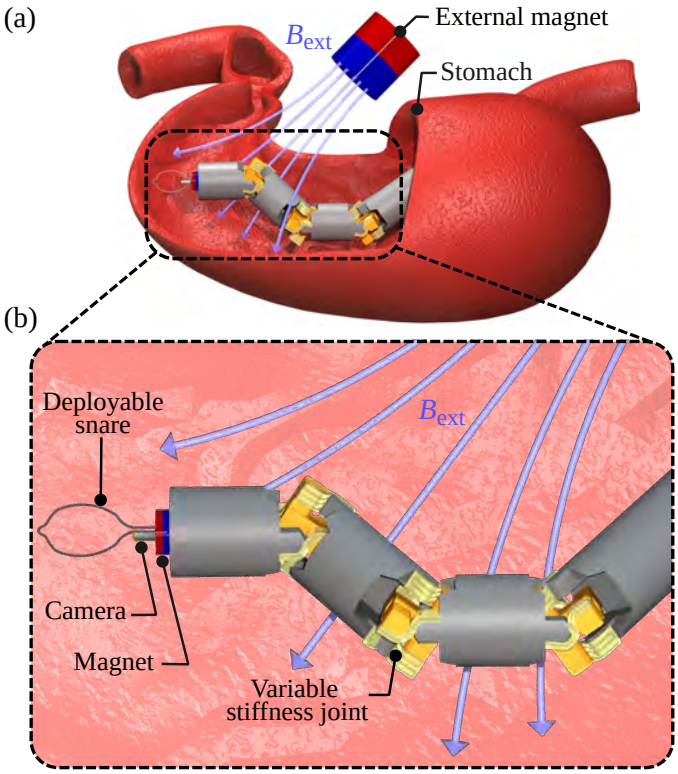

Fig. 1. (a) The 6-degree-of-freedom manipulator is steered inside a stomach phantom by changing the external magnetic field (B_{ext}), thereby actuating the permanent magnet attached at the tip (stomach model adapted from [9]). (b) The design concept consists of a series of variable stiffness universal joints employing shape memory polymer. Each joint allows deflection in the soft state and shape-locking in the stiff state. A camera and a deployable snare positioned in the working channel are used to inspect and remove tissue.

A great number of flexible manipulator concepts are tendon-driven [3], [10]–[12], pneumatic-driven [13], or employ a combination of both [7]. Tendon-driven systems offer high flexibility and can generate large forces at the end-effector. Nevertheless, they suffer from cable friction and backlash hysteresis [14]. On the other hand, pneumatic systems are lightweight [15], [16], but are challenging to miniaturize and the actuation channels pose the risk of being pinched during bending. Additionally, both methods are limited to pre-defined degrees of freedom (DOFs) that are built into the manipulator. In contrast, magnetic actuation systems eliminate the need for actuators routed inside the manipulator that could cause cable friction or space limitations. Magnetic actuation also offers up to five DOFs per magnet, thus providing more orientation options for manipulation [17]. The human body is perme-

This article has been accepted for publication in IEEE Transactions on Medical Robotics and Bionics. This is the author's version which has not been fully edited and content may change prior to final publication. Citation information: DOI 10.1109/TMRB.2024.3464668

able to magnetic fields, making this approach suitable for medical applications. A magnetic actuation system typically consists of electromagnetic coils or permanent magnets that can generate magnetic fields interacting with magnets embedded in manipulators [18]–[20]. These fields can be applied using robot-mounted permanent magnets to actuate continuum robots [21], or using electromagnets to precisely manipulate a flexible needle for neurosurgical procedures [22]. Other studies have shown flexible joints built in surgical end-effectors with embedded magnets controlled by external magnetic fields [5], [23]. Pittiglio *et al*., developed a hyper-redundant robot based on a concatenation of permanent magnetic spheres to achieve sharp bends of 165 ° [24]. However, the independent control of multiple permanent magnets embedded in a manipulator to achieve distinct DOFs remains challenging.

Selective stiffening and softening of joints or segments can allow for control of individual DOFs in an otherwise underactuated system. Stiffening strategies based on layer and fiber jamming are difficult to miniaturize but have been used to design snake-like variable stiffness manipulators [25], [26]. Electromagnetic gear locking has also been proposed alongside tendon-driven actuators for a laparoscopic tool, which suffers from cable friction and gear backlash [27]. Another stiffness regulation strategy is the use of variable stiffness (VS) materials such as low melting point alloys (LMPAs), shape memory alloys (SMAs), and shape memory polymers (SMPs). These materials exhibit significant changes in stiffness in response to external stimuli such as heat [28]–[30]. The rapid stiffness change of LMPA was exploited to design continuum devices for MIS [31], [32]. However, the toxicity of LMPA poses a health risk and requires safe encapsulation. SMAs provide bio- and magnetic compatibility and have been used as heat-sensitive actuators to design compliant joints suitable for magnetic resonance [33]. Despite this, SMA actuators primarily use their shape memory effect for actuation, offering limited shape variety and low stiffness variability. [14]. Compared to SMAs, SMPs exhibit greater stiffness variation, are compatible with 3D-printing techniques [34], and allow multiple transition points close to human body temperature [35]. SMPs differ from regular polymers in their enhanced cross-linking, allowing them to lock into a shape or revert to their original form after deformation. Given these attributes and their ease of fabrication, SMPs have emerged as a frequently used material to design VS devices.

Magnetically-actuated catheters primarily made out of SMP that can be shape-locked in space when needed have been shown with active and passive cooling [36]–[38]. However, entirely SMP-based designs with flexible bending sections cannot selectively lock specific DOFs, thus compromising lateral support stiffness when heated. In addition, the number of working channels is limited due to smaller diameters (Table I). Fukushima *et al*., studied a manipulator with discrete joints enclosed by SMP collars. This enables selective fixation and actuation along 2-DOFs but requires both pneumatic and tendon-driven systems for actuation [7]. Firouzeh *et al*., introduced a tendon-driven robotic gripper featuring buckling joints actuated by Joule heating [39], [40]. While this design employs SMP for variable stiffness, it is confined to 1-DOF joints. Consequently, enabling multiple DOFs at a single joint location would make a manipulator more maneuverable and compact. The universal joint (U-joint) is a compact mechanical connection widely used as a 2-DOF joint in industrial robotic manipulators [41]. Manfredi and Cuschieri designed a miniature 2-DOF U-joint actuated by wires. However, it is limited to a range of motion (ROM) of 30 °, exhibits cable friction, and its applicability to serial joints is untested [29].

This work presents a magnetically-actuated U-joint, capable of variable stiffness behavior through SMP. The schematic in Fig.1 shows an arrangement of U-joints in series forming a 6-DOF manipulator (6DM). The 6DM is magnetically steerable with independently addressable DOFs. Each DOF can be controlled by applying an external magnetic field to a permanent magnet attached to the tip of the 6DM. This eliminates the need for actuators routed inside the manipulator. The 6DM is designed for maneuverability and can avoid obstacles in confined spaces. Tools can be positioned in working channels to serve as surgical instruments. Using flexure-based rolling contact, the design benefits from a reduced part count, simpler manufacture, and is not susceptible to buckling. A novel fabrication process is used to produce VS-flexures with embedded heating elements. Each DOF can be independently softened or shape-locked within a short time (Table I). The VS-flexures are shape-retrained to ensure a stable assembly even when heated. Finally, a prototype of a 6DM is fabricated. It can independently control multiple 2-DOF joints in series with a single permanent magnet. The modular design allows the number of DOFs to be customized. This allows the manipulator to adopt a serpentine pattern to circumvent obstacles and access hard-to-reach surgical sites. The spatial maneuverability of the 6DM is demonstrated in a workspace with obstacles, while its surgical use is illustrated through a polypectomy operation.

The paper is structured as follows: Section II covers the design, kinematics, actuation principle, and fabrication of the U-joints and 6DM. Section III characterizes the thermal, mechanical, and thermomechanical properties, followed by demonstrations of the 6DM in a practical surgical scenario. Section IV discusses the results. Section V concludes the paper with an emphasis on future work.

II. Materials and Methods

A. Design Concept

The primary functional element is a 2-DOF U-joint (Fig. 2(a)). A U-joint, often referred to as a Hooke's joint or Cardan joint, is a coupling mechanism that links misaligned axes and is commonly used in shafts transmitting rotary motion [42]. The proposed U-joint consists of three main components: two yokes and a cross-link. The yokes are connected at right angles to the cross-link by flexures made of SMP. The flexures have an S-shape that holds the yokes and cross-link together through rolling contact (Fig. 2(a)). This prevents the flexures from buckling and provides axial shape retention between the yokes and the cross-link. Heating these flexures using embedded heating elements allows for variable stiffness, i.e. flexible bending and shape-locking. The joint

TABLE I
COMPARISON WITH MAGNETICALLY-ACTUATED MANIPULATOR DESIGNS BASED ON VARIABLE STIFFNESS (VS) MATERIALS

Ref	Type	VS material	Actuation time [s](1)	Range [°]	OD [mm]	Channels	DOF locking (2)	Modular
[36]	Continuum	SMP (MM4520)	18 / 90	90	2	1	No	No
[37]	Continuum	SMP (MM5520)	13 / 115	127	2.3	1	No	No
[32]	Continuum	LMPA (Cerrolow117)	15 / 80	100	2.33	1	No	No
[38]	Continuum	SMP (NOA63)	7 / 59	60	2.5	1	No	No
[30]	Continuum	SMP (MP3510)	20 / 240	180	10	1	No	Yes
This work	**Discrete joints**	SMP (MP3510)	**14 / 64**	**127**	**12**	**4**	**Yes**	**Yes**

(1) Two actuation times are provided for thermal actuation (heating time/cooling time). For cooling, only values for passive cooling are considered in this comparison. (2) Refers to the ability to lock individual degrees of freedom within a joint or segment having multiple degrees of freedom.

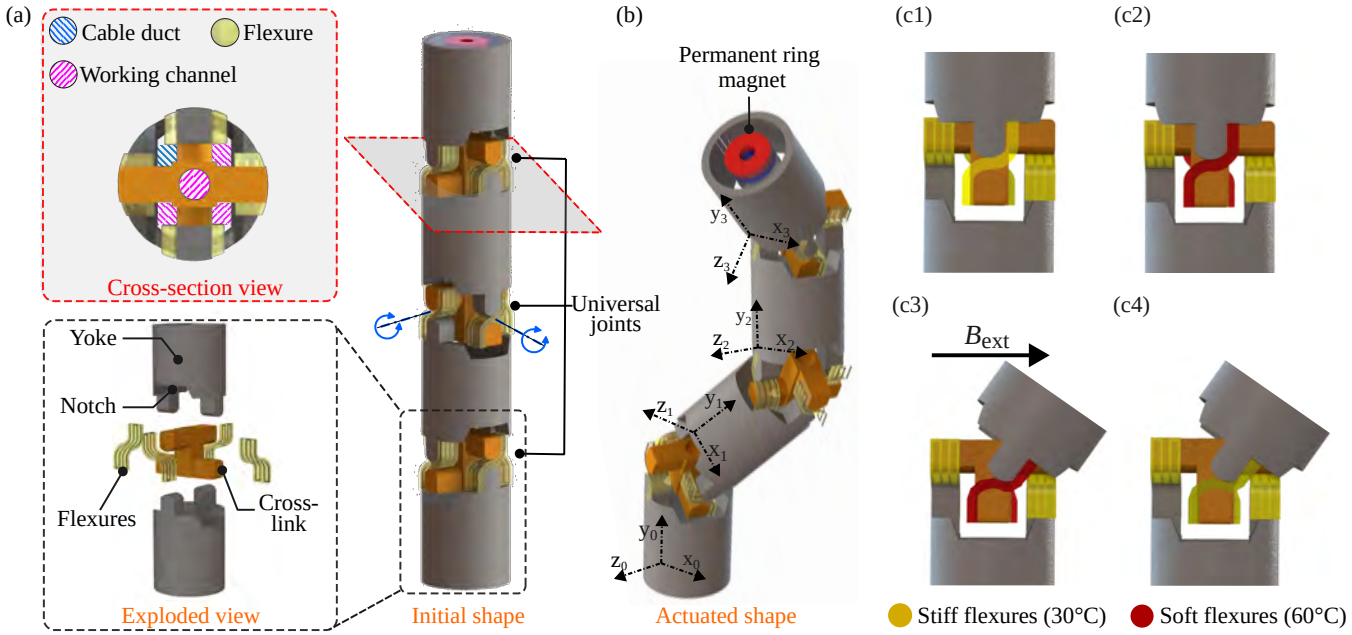

Fig. 2. (a) Assembly of the universal Joint (U-Joint) forming the 6-degree-of-freedom manipulator (6DM). Each U-joint consists of two yokes and a cross-link connected by flexures. Rolling contact between the yoke and cross-link enables rotation about two axes. In the initial shape, all six degrees of freedom (DOF) are constrained. (b) By successively heating, deflection, and cooling joints 1-3, the 6DM takes on complex shapes as illustrated by the reorientation of the coordinate frames. x_i, y_i, z_i indicate the local coordinate frames of each joint. (c1)-(c4) Actuation principle of the U-Joint with heated flexures indicated by red coloring. (c1) In the initial shape, no flexure is actuated, and both DOFs of the joint are restricted. (c2) One pair of flexures is heated by the embedded heating element and becomes soft. (c3) In the soft state, the flexure pair can be deflected by an external applied magnetic field (B_{ext}) along the corresponding DOF. (c4) Due to ambient convection, the flexure pair cools down and regains its stiffness and the joint is fixed at the current bending angle.

allows a selective actuation of 2-DOFs along intersecting axes of rotation (pitch and yaw) with a ROM of 60 ° each. A notch on both sides of the yoke allows it to rotate freely without coming into contact with the cross-link. The joint's cross-section includes a central working channel and four off-center working channels, one of which is designated as a cable duct for the SMP actuators (Fig. 2(a)). The working channels are non-continuous with openings between sections, where tools can be positioned in advance. The design is modular and can be extended by plug-in connections to form a manipulator with 6-DOFs. A ring magnet attached at the distal end of the 6DM enables contactless actuation.

B. Kinematic Analysis

A forward kinematics analysis for the 6DM is performed using the Denavit-Hartenberg (DH) convention [43]. It outlines four DH parameters that describe the frame assignment to each link of the 6DM (Table II).

TABLE II
DENAVIT-HARTENBERG PARAMETERS FOR THE 6-DOF MANIPULATOR

Frame	$\alpha_{i-1}[rad]$	$d_i[mm]$	$l_{i-1}[mm]$	$\theta_i[rad]$
1	0	0	0	0
2	0	0	$l_1 = 18$	θ_1
3	-$\pi/2$	0	0	θ_2
4	$\pi/2$	0	$l_2 = 22$	θ_3
5	-$\pi/2$	0	0	θ_4
6	$\pi/2$	0	$l_3 = 22$	θ_5
7	-$\pi/2$	0	0	θ_6
8	0	0	$l_4 = 18$	0

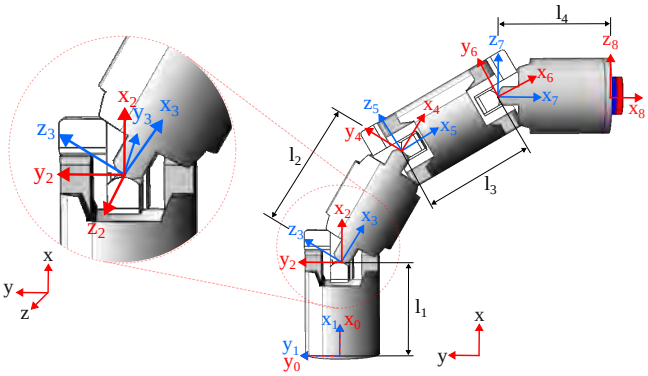

Fig. 3. Kinematic analysis of the 6-DOF manipulator with two frames attached to each joint.

Fig. 3 shows the allocation of reference frames. Given the two rotation axes per U-joint, two reference frames are positioned between adjacent yokes.

The DH transformation matrix is structured as

$$T_i^{i-1} = \begin{bmatrix} c(\theta_i) & -s(\theta_i) & 0 & l_{i-1} \\ s(\theta_i)c(\alpha_{i-1}) & c(\theta_i)c(\alpha_{i-1}) & -s(\alpha_{i-1}) & -s(\alpha_{i-1})d_i \\ s(\theta_i)s(\alpha_i) & c(\theta_i)s(\alpha_{i-1}) & c(\alpha_{i-1}) & c(\alpha_{i-1})d_i \\ 0 & 0 & 0 & 1 \end{bmatrix} \tag{1}$$

where $c(\theta_i)$ and $s(\theta_i)$ represent the cosine and sine of θ_i respectively. T_i^{i-1} denotes the transformation matrices from the $(i-1)$th to the succesive ith link of the manipulator.

To compute the homogeneous transformation matrix from the base to the end-effector, the individual transformation matrices are composed in Eq.(2).

$$T_8^0 = T_1^0 T_2^1 \dots T_8^7 \tag{2}$$

The spatial coordinates of the end-effector are denoted as $[X_E\ Y_E\ Z_E]$, and consequently the final end-effector position (P_E), can be determined using Eq. (3).

$$P_{\mathrm{E}} = \begin{bmatrix} X_{\mathrm{E}} \\ Y_{\mathrm{E}} \\ Z_{\mathrm{E}} \\ 1 \end{bmatrix} = T_8^0 \cdot \begin{bmatrix} 0 \\ 0 \\ 0 \\ 1 \end{bmatrix} \tag{3}$$

The rotation matrix $R = T_8^0(1:3, 1:3)$ of the composite transformation matrix T_8^0 is extracted to analyze the maximum angle of deviation between the initial and final orientations of the end effector. Fig. 4(a1)-(a3) show the configuration possibilities that can be achieved through successive joint actuation from distal to proximal. Fig. 4(b) depicts the maximum 3D workspace using 6-DOFs. The surface diagram in Fig. 4(c) displays the maximum bending angle as a function of uniform pitch and yaw angles across the U-joints. As can be seen, a single actuated DOF (pitch = 30 °, yaw = 0 °) across all U-joints yields a maximum bending angle of 90 °. With two actuated DOFs per U-joint (pitch = 30 °, yaw = 30 °), this angle extends to ≈127 °.

C. Actuation Principle

Thermo-responsive SMP exhibits variable stiffness properties by the interaction between polymer chains on a molecular level. In the glass phase, the chains are locked by intermolecular interactions, resulting in a rigid structure. In the rubber phase, the intermolecular forces weaken, allowing the chains to move more freely and the material to become flexible [44].

This material property is exploited in the actuation principle of the joint, as illustrated in Fig. 2(c1)-(c4). In the initial state, no flexure is heated (SMP temperature $\leq 30\,^{\circ}$C) i.e., both DOFs are restricted (Fig. 2(c1)). At this point, the 6DM exhibits no DOFs (Fig. 2(a)). When a pair of opposing flexures are heated and become soft by Joule heating (SMP temperature $= 60\,^{\circ}$C), the corresponding DOF is unlocked (Fig. 2(c2)) and the joint can be deflected by an external magnetic field (B_{ext}) acting on the embedded magnet (Fig. 2(c3)). After cooling through ambient convection, the flexures regain their stiffness (SMP temperature $\leq 30\,^{\circ}$C) , and the joint is shape-locked at the current bending angle (Fig. 2(c4)). This process can be repeated with the second pair of flexures within the same U-joint, allowing the independent control of two DOF per joint. Through this, the 6DM can adopt various shapes using a single magnet by successively heating, deflecting, and cooling joints 1, 2, and 3 as displayed in Fig. 2(b). Alternatively, two pairs of flexures within a single U-joint can be actuated together, unlocking two DOFs simultaneously.

The deflection can be induced by a torque generated at the tip of the manipulator where a ring-shaped magnet is attached. An external magnetic field can be generated either through electromagnetic coils or by a permanent magnet. In this study, the characterization and obstacle navigation experiments are performed in a system that comprises six electromagnetic coils arranged in a Helmholtz configuration, providing a cubic workspace (60 x 60 x 60 mm) for magnetic manipulation. This system can generate a homogeneous magnetic field of up to 55 mT in any chosen orientation [4]. It can be assumed that the magnetic field gradient's effect is negligible. Hence, the resulting bending moment acting on the joint is primarily due to magnetic torque (T) as given by

$$T = \mu B \sin(90^{\circ} - \alpha) \tag{4}$$

where μ is the magnetic dipole moment from the permanent magnet, alpha (α) is the deflection angle of the joint, and B denotes the external applied magnetic field. Consequently, the deflection can be increased by increasing the field magnitude.

D. Fabrication

The VS-flexures are made of custom-designed heating elements embedded between two sheets of SMP. To fabricate the SMP sheets, DiaPLEX MP3510 (SMP Technologies Inc., Shibuya City, Japan) with a thermal conductivity of 0.20 W/(mK) at 23 °C is used. This material is provided as a two-part potting compound. Both the resin and hardener are placed in equal proportions in a 50 ml dual cartridge (Adhesive Dispensing Ltd., U.K.) and then degassed

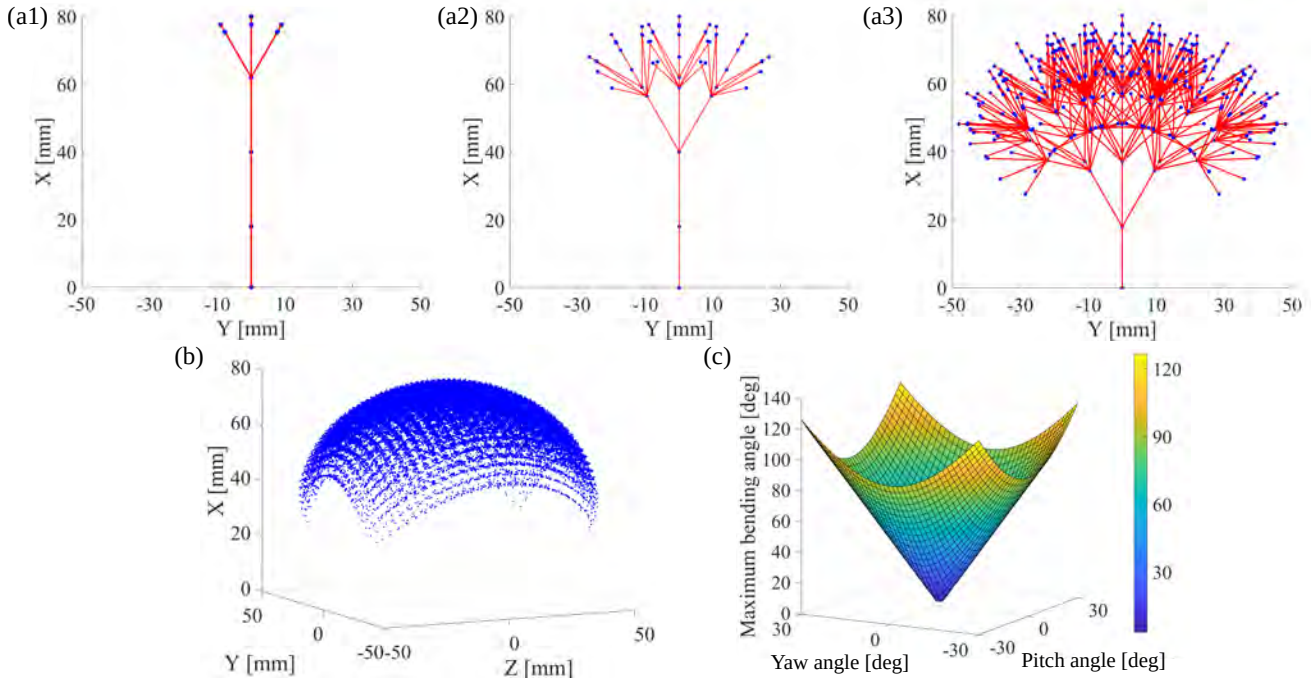

Fig. 4. (a1)-(a3) Configuration possibilities in 2D view of the 6-DOF manipulator through successive joint actuation from distal to proximal. Linkages are colored red and end-effector positions are marked with blue dots. (b) The corresponding 3D workspace of the end-effector tip when all DOFs are active. (c) Surface diagram with the maximum bending angle as a function of uniform pitch and yaw angles across all universal joints of the 6-DOF manipulator.

in a vacuum chamber (<10 Pa) for 2 hours (Fig. 5(a)). Next, the two components are mixed in a 1:1 volume ratio using an MBH04-12D mixer nozzle (Adhesive Dispensing Ltd., U.K.) and then injected into a Polymethyl methacrylate (PMMA) mold (Fig. 5(b)). Immediately after, the mold is placed into an oven and cured at 70°C for 2 hours. Post-curing, the SMP sheets are cut out of the mold in rectangular sheets (3.5 x 8 x 0.5 mm) using a laser cutter (Laser engraving system Speedy 300, Trotec Ltd.) as shown in Fig. 5(c).

To fabricate the heating element, a thin foil (20 μm) made of stainless steel (material no. 1.4301) with an electrical resistance of $0.072 \times 10^{-6}\,\Omega$m and thermal conductivity of 16.2 W/(mK) at 20 °C is used to achieve high-resistance. To increase the resistivity, a serpentine path is laser cut into the foil as shown in Fig. 5(d). This serpentine path forms an electrical circuit loop with a total resistance of 2.3 Ω. To form the complete VS-flexure, the heating element is placed between two SMP sheets and heat pressed together for 60 s at 80 °C (Fig. 5(e)). The dimensions of the heating element can be inferred from Fig. 5(f). The primary shape of the flexure is retrained to an S-shape through extended heating at 70 °C for 20 hours. By this, molecular disturbances from residual strain can be removed, as observed in multiple studies on SMP shape-retraining [45]. Afterward, electrical wires for the power supply are connected to the heating element. To prevent cable tension, a slack length is provided.

The assembly of the 6DM is shown in Fig. 6. The VS-flexures are attached to the cross-link and the yokes by an adhesive bond (LOCTITE 401, Henkel Adhesive Technologies). The cross-link and the yokes are 3D-printed with Acrylonitrile Butadiene Styrene (ABS). When assembled, the 6DM weighs 6 g with an outer diameter of 12 mm and a total length of 80 mm (Fig. 6). At the distal end, two stacked axially magnetized N45 neodymium ring magnets (Neomagnete, Germany) measuring 6 x 2 x 2 mm are embedded.

III. Experiments and Results

First, the SMP material is thermomechanically analyzed, followed by a thermal characterization of the VS-flexure using thermal imaging. Then, the stiffness, shape-locking capability, and actuation behavior of the joint are characterized by magnetically induced deflections within the Helmholtz configuration (II-C). Each property is tested separately on a 1-DOF version of the U-joint with an embedded magnet, as outlined in subsections III-A–III-G. Finally, the selective actuation, maneuverability, and application of the 6DM is demonstrated in III-H–III-J.

A. Thermomechanical Characterization

1) Experimental Setup: The elastic modulus in polymers depends on temperature and the strain rate. To assess the thermomechanical properties of the SMP used, a dynamic mechanical analysis is conducted (EPLEXOR 2000, Gabo Qualimeter Testanlagen GmbH). This technique measures the effects of strain rate and temperature on the elastic modulus. Initially, a static load is applied to the test samples, followed by the application of sinusoidal mechanical vibrations at a frequency of 1 Hz. The temperature gradually rises from 0 °C to 80 °C in increments of 2.5 °C per minute.

This article has been accepted for publication in IEEE Transactions on Medical Robotics and Bionics. This is the author's version which has not been fully edited and content may change prior to final publication. Citation information: DOI 10.1109/TMRB.2024.3464668

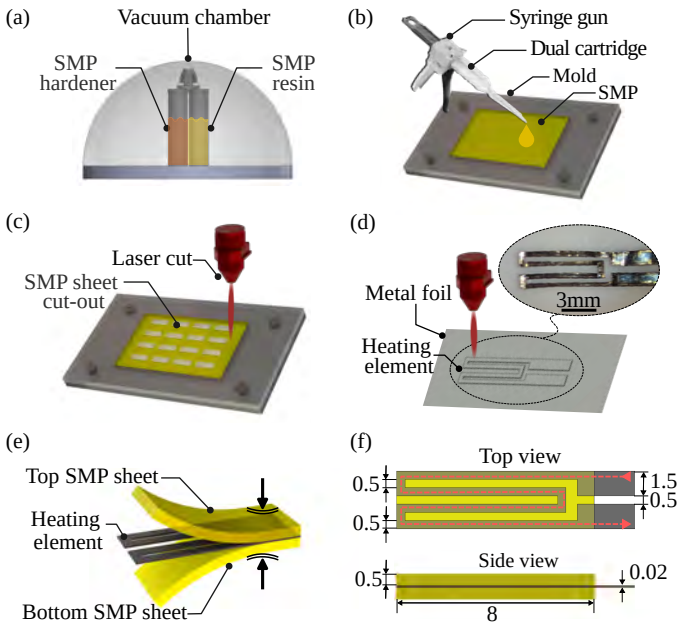

Fig. 5. Illustration of the fabrication process of a variable stiffness (VS) flexure. (a) Shape memory polymer (SMP) components are placed into a vacuum chamber for 2 hours. (b) SMP components are mixed in a 1:1 ratio using a syringe gun and injected into a mold, then cured for 2 hours at 70 °C. (c) SMP sheets are cut out of the mold using a laser cutter. (d) The flexible heating element is cut out of a metal foil using a laser cutter. **(e)** The heater element is pressed between two sheets of SMP. (f) The complete VS-flexure with the heating element embedded. The dashed red line indicates the current flow. Dimensions are in mm.

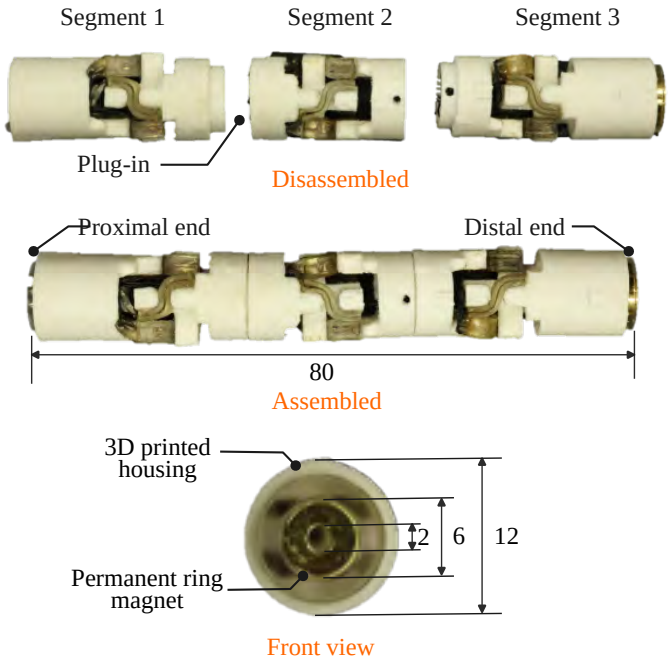

Fig. 6. The prototype of the 6-degree-of-freedom manipulator is shown in a dissembled and assembled configuration using plug-in connections to achieve a modular assembly. The yokes and cross-link are 3D-printed with Acrylonitrile Butadiene Styrene. The front view displays the NdFeB ring-shaped magnet fixed at the distal end of the manipulator. At the proximal end, surgical tools can be inserted through a working channel. Dimensions are in mm.

2) Results: The result of the thermomechanical characterization of the SMP is shown in Fig. 7(a)). As the temperature increases from 0 ° to 80 °C, the elastic modulus of the SMP experiences a reduction from E_{Stiff}≈1.57 GPa to E_{Soft}≈8 MPa. Most of this change in stiffness is observed in a temperature range centered around the transition temperature (T_g= 35 °C), which is identified as the transition region. At 30 °C, the SMP is considered to be in the stiff state, while at 60 °C it is considered to be in the soft state as it enters the rubber region.

B. Thermal Characterization

1) Experimental Setup: To operate the U-joint effectively, understanding the temperature variations of the VS-flexure at different currents is crucial. To collect the heating and cooling curve of the VS-flexure, the terminals are connected to a precision DC bench power supply (TSX3510, UK). An infrared camera (Fluke Ti400, Washington, USA) captures the temperature readings. Different electric currents are applied until the actuation temperature of 60 °C is reached. This is followed by cooling through ambient convection at a room temperature of ≈25 °C. Each test was repeated 3 times to ensure statistical reliability

2) Results: Fig. 7(c),(d) show the thermal camera images and the corresponding temperature profile of a VS-flexure measured by the infrared camera. The VS-flexure needs 14 (±0.8), 21 (±1), 38 (±1.9), and 124 (±6.7) s to be fully softened (60 °C) when currents of 0.4, 0.35, 0.3, and 0.25 A are applied, resulting in power outputs of 0.37, 0.28, 0.21, and 0.14 W, respectively. Conversely, it takes

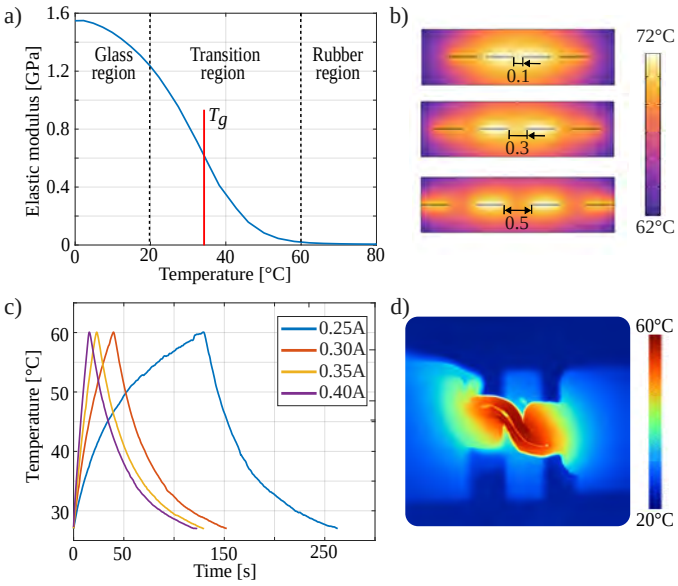

Fig. 7. (a) The elastic modulus versus temperature of the SMP material is measured using a dynamic mechanical analyzer. The transition temperature (T_g) is 35 °C. (b) Heat model of the cross-sectional spatial temperature distribution of a heating element embedded between two sheets of SMP with varying path distances. (c) Temperature profile of the variable stiffness flexure measured by the thermal camera over time at applied currents of 0.25, 0.3, 0.35, and 0.4 A. (d) Thermal camera image of the actuated flexure.

64 (±3.7) s for the VS-flexure to cool down to 30 °C. The results show that higher currents can significantly reduce heating time. In Fig. 7(b), a 2D heat transfer simulation (COMSOL Multiphysics 6.0. COMSOL, Inc.) illustrates the effect of varying path distances of the heating element on the cross-sectional spatial temperature profile of a VS-flexure. The temperature profile is shown after 10 s with a heat output of 0.2 W, and a heat transfer coefficient of 60 W/(m^{2}K). The model demonstrates how the distance between the heating paths is fine-tuned to 0.5 mm to ensure a uniform heat distribution.

C. Bending Stiffness

1) Experimental Setup: To characterize the stiffness in both intended and parasitic motion, the deflection is measured in two planes relative to the VS-flexure. The principal bending plane is characterized by the principal axis of flexibility (XY-plane in Fig. 8(a)). The lateral bending plane is perpendicular to the principal bending plane and offers higher resistance to bending deformation (ZY-plane in Fig. 8(b)). Bidirectional deflections in stiff and soft states are measured during the application of a magnetic field cycle $B_{\text{ext}} \in [-20\,\text{mT}, 20\,\text{mT}]$. Image tracking is done using a camera (FLIR Blackfly S USB3 camera, USA). The joint deflection is quantified using the Image Processing Toolbox in MATLAB R2023A.

2) Results: In the principal bending plane, the maximum deflection in the soft state [-30 °,32 °] changes to [-3 °,4 °] in the stiff state as shown in Fig. 8(a). This corresponds to a change in stiffness from 0.57 Nmm/° (stiff) to 0.06 Nmm/° (soft) demonstrating the effective tunability of the joint's stiffness. In the soft state, hysteresis is observed with an angular deviation of 20 ° between loading and unloading (Fig. 8(a)). In the lateral bending plane, the deflection in the soft state [-5 °,5 °] significantly exceeds that in the stiff state [-0.5 °,0.5 °] (Fig. 8(b)). The results are summarized in Table III.

D. Torsional Stiffness

1) Experimental Setup: By repositioning the embedded magnet within the joint, an axial torque can be induced in response to a magnetic field of $B_{\text{ext}} \in [0\,\text{mT}, 20\,\text{mT}]$. The torsional deflection angle (β) of the joint is measured using a protractor tool.

2) Results: A magnetic field of 20 mT induces a maximum torsion of 20 ° in the soft and 1 ° in the stiff state (Fig. 8(c)).

E. Current-Responsive Actuation

1) Experimental Setup: In Fig. 8(d), unidirectional deflection in the soft state is measured over time when a constant magnetic field of 20mT is applied at currents of 0.25, 0.3, 0.35, and 0.4 A. The different currents are continuously applied until the deflection reaches a plateau.

2) Results: When applying currents of 0.3, 0.35, and 0.4 A, the deflection reaches its plateau after 43, 30, and 22 s, respectively. In contrast, an applied current of 0.25 A fails to fully actuate the SMP, demonstrating that the rate of deflection can be influenced by the amount of current applied.

F. Shape-Locking

The shape-locking capability of a sequential arrangement of joints requires each joint to maintain its deflection in a locked state, even when a magnetic field is applied.

1) Experimental Setup: In this experiment, a single DOF is repeatedly actuated (soft state) and then deflected by $B_{\text{ext}} \in \{0\,\text{mT}, 5\,\text{mT}, 10\,\text{mT}, 15\,\text{mT}, 20\,\text{mT}\}$ corresponding to I-V in Fig. 8(e). The joint then cools down and is shape-locked, while the magnetic field remains active. Following this, a magnetic field of -20 mT and +20 mT is applied for 30 s in each case to measure the bidirectional deflection from a deflected initial position.

2) Results: At various initial shape-locked positions (Fig. 8(e) I-V), the joint shows deflections of less than 4 °. A continuous decrease in deflection from I-V can be observed, indicated by the red error bars. The maximum deflection [3.4 °, 3.9 °] (at position I) occurs when there is no initial deflection, resulting from the magnet's orientation being at its maximum angle relative to the external magnetic field. At this point, a bending moment of 2.26 Nmm is applied. This experiment proves that the joint maintains consistent shape-locking stability across different angular positions.

G. Oscillating Actuation

1) Experimental Setup: In Fig. 8(f), the joint is exposed to a magnetic field $B_{\text{ext}} \in [-20\,\text{mT}, 20\,\text{mT}]$ that oscillates at a frequency of 1 Hz. The deflection angle (blue graph, left Y-axis) and the temperature (red graph, right Y-axis) are both plotted against time (X-axis). Currents of 0.3 A are applied for 30 s until the rubber phase is reached.

2) Results: After 30 s, the temperature and deflection peak at their maximum, being 60°C and 30°. In the following, the joint cools down to 30 °C and the angular deflection levels off at 2.5 °. The data indicates that the ROM can be dynamically controlled by the applied current and the resultant temperature profile.

H. Selective Joint Actuation

The 6DM can adopt serpentine shapes by a serial actuation of joints in multiple directions using a single magnet. The diagram in Fig. 9(a1) shows the joints 1, 2, and 3 following the sequential actuation, deflection, and shape-locking of the initially straight 6DM to take on a serpentine pattern. The deflection angle at each joint is measured with respect to the previous joint segment. Joint 1 is heated and bends downwards by applying a magnetic field of -20 mT. After deflection, joint 1 is shape-locked (Fig. 9(a1) top image). Next, joint 2 is made flexible, bent upwards using +20 mT, and then shape-locked (Fig. 9(a2) middle image). Finally, joint 3 is manipulated downwards by applying again a magnetic field of -20 mT and then shape-locked (Fig. 9(a3) bottom image). When the first joint is deflected, all following joints bend in sync because joints 2 and 3 remain stiff. Consequently, when joint 2 deflects in the opposite direction, joint 3 bends in sync. Upon deflection of joint 3, joints 1 and 2 remain stiff. In Fig. 9(a3), the step functions represent the applied currents and magnetic fields.

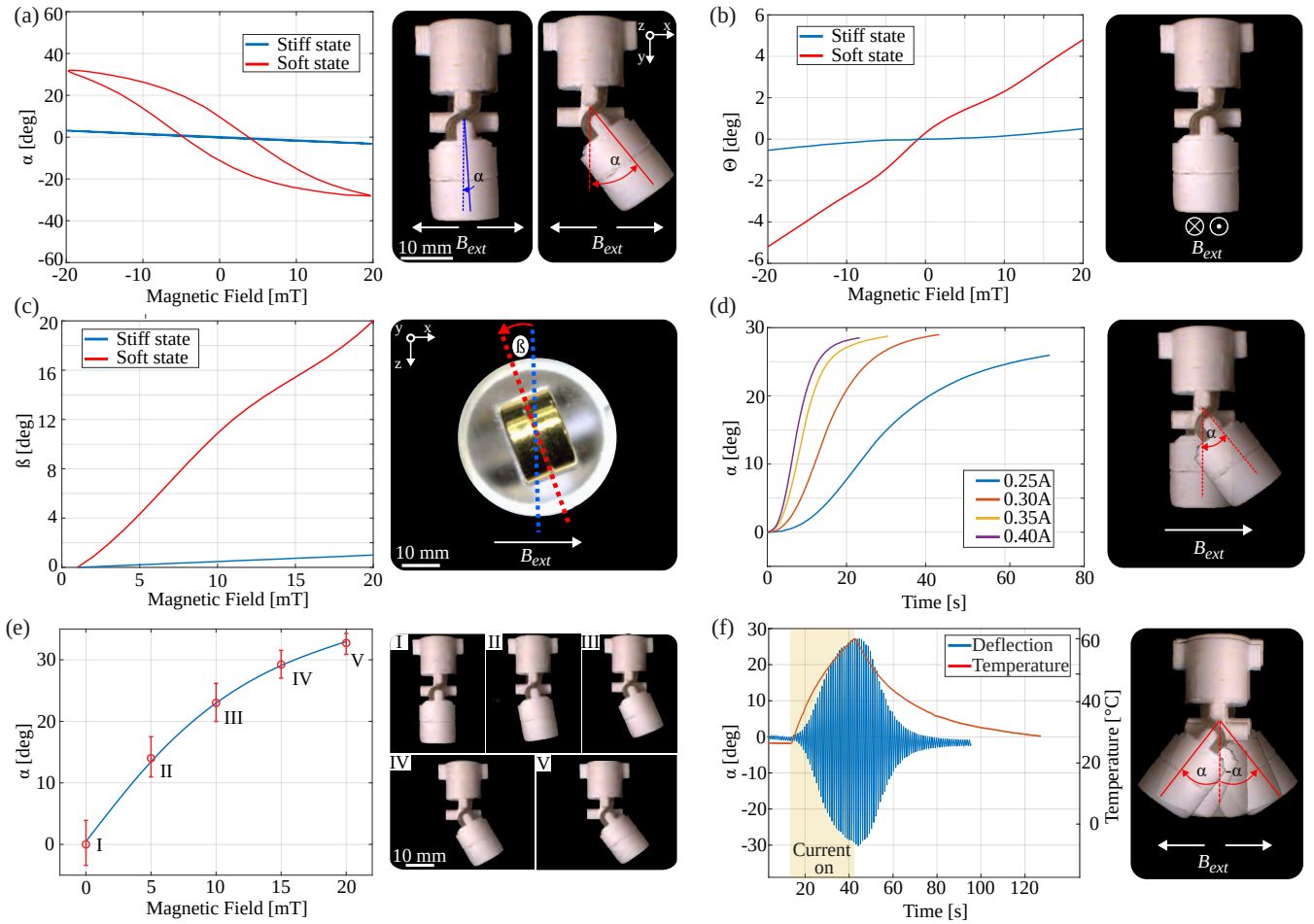

Fig. 8. (a) Deflection along the principal bending plane (α) versus magnetic field (B_{ext}) measured in soft and stiff states. (b) Deflection perpendicular to the principal bending plane (Θ) versus B_{ext} measured in soft and stiff states. (c) Unidirectional torsion (β) versus B_{ext} in $[0\,\text{mT}, 20\,\text{mT}]$ measured in soft and stiff states. The view is from the bottom of the joint. (d) Deflection induced by a constant B_{ext} in $\{20\,\text{mT}\}$ at applied currents of 0.25, 0.3, 0.35, and 0.4 A. (e) The joint is shape-locked (stiff) at different deflected positions caused by B_{ext} in $\{0\,\text{mT}, 5\,\text{mT}, 10\,\text{mT}, 15\,\text{mT}, 20\,\text{mT}\}$. Subsequently, B_{ext} in $\{-20\,\text{mT}, 20\,\text{mT}\}$ is applied to measure bi-directional deflection indicated by red error bars from a deflected initial position in the stiff state. (f) The range of motion and temperature is measured dynamically over time when a current of 0.3 A is turned on after 10 s and turned off after 30 s while a continuously oscillating B_{ext} in $[-20\,\text{mT}, 20\,\text{mT}]$ is applied at 1 Hz.

The data is captured from the video footage. Please refer to the supplementary video to see the sequential actuation and locking of joints. In Fig. 9(b1) a constant load (weight of 10 g) is applied to the tip of the 6DM. Sequentially softening one DOF per joint from distal to proximal induces a vertical tip deflection (Y-axis left) and a bending angle from base to tip (Y-axis right). The experiment is repeated three times with error bars representing the standard deviation. Following the actuation of three DOFs across three joints, the radius of curvature measures 55 (±3.4) mm, alongside a maximum deflection angle of 90 (±1.5) ° as shown in Fig. 9(b2).

I. Obstacle Avoidance

This experiment for obstacle avoidance within a confined space illustrates the maneuverability of the 6DM in challenging terrains. A PMMA container ($10\times8\times4$ cm) serves as a test site inside the workspace of the Helmholtz configuration (II-C). Inside the container, four PMMA rods are arranged at right angles and form obstacle grids. As a target, a 3D-printed sphere representing a polyp (8 mm in diameter) is attached to one of the rods at the right end of the container. Two cameras capture both overhead (top view) and lateral (side view) perspectives of the manipulator's actions. The bending direction (left and right, up and down) can be controlled using the magnitude and direction of the magnetic field. When using all 6-DOF, the 6DM can be controlled to navigate the obstacles and reach the target as shown in Fig. 10. The forward motion is achieved using a linear slide. Please refer to the supplementary video to see the obstacle navigation.

J. Application Demonstration

To investigate the utility of the 6DM in a practical scenario, the detection and removal of a polyp from a stomach phantom is simulated. Gastric polyps are unusual growths that emerge on the stomach's interior surface, which can pose a health risk if not addressed. These growths are typically identified through an endoscopic examination (gastroscopy), where a flexible instrument with a small camera attached is navigated in the stomach to visually inspect the area [46]. Subsequently, polyps can be resected using specialized biopsy tools (polypectomy).

This article has been accepted for publication in IEEE Transactions on Medical Robotics and Bionics. This is the author's version which has not been fully edited and content may change prior to final publication. Citation information: DOI 10.1109/TMRB.2024.3464668

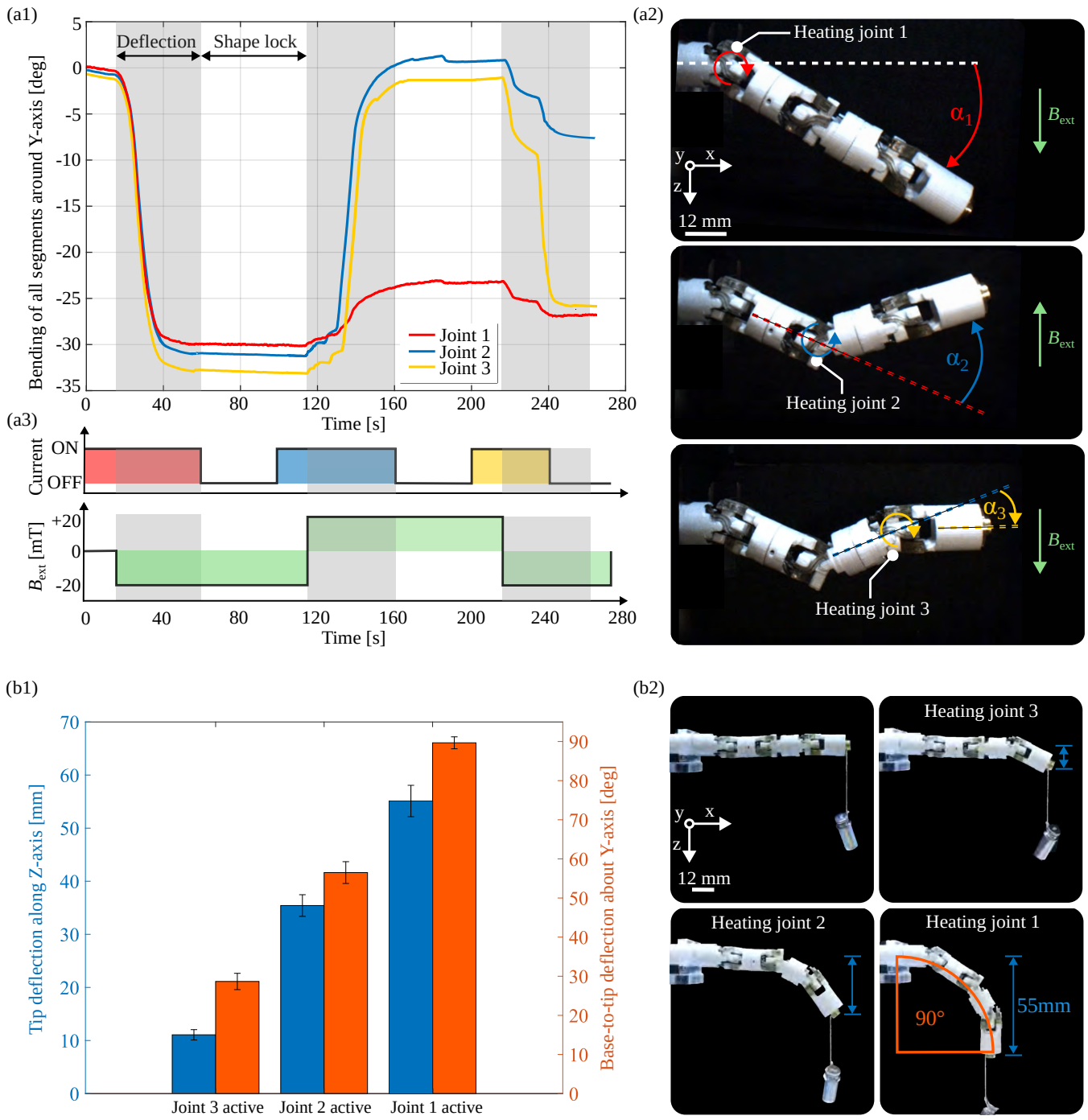

Fig. 9. (a1) The deflection angles of joints 1, 2, and 3 are measured over time to demonstrate sequential deflection and shape-locking. The first and third joints bend downwards, while the second joint bend upwards, forming a serpentine pattern. (a2) Snapshots of each joint deflection. (a3) Step functions for the current supply and magnitude of the magnetic field (B_{ext}). After full actuation (60 °C) by currents of 0.3 A, a magnetic field of -20 mT is applied to cause deflection in joints 1 and 3, while a magnetic field of +20 mT is used for joint 2. (b1) The vertical tip and angular base-to-tip deflection is measured under a constant load. Error bars represent standard deviation. (b2) Joint actuation from distal to proximal with a 10 g weight attached to the tip.

For the gastroscopic demonstration, an N45 neodymium cylinder magnet with a diameter of 30 mm and a height of 40 mm is used to generate the external magnetic field and manipulate the 6DM. During this test, the magnet is maneuvered by hand and kept at a distance of 100 to 60 mm from the 6DM, which generates magnetic fields ranging from 5 to 20 mT. For visual inspection, a camera with a diameter of 0.91 mm (Misumi Electronic Corporation, Taiwan) is used. For the polypectomy demonstration, a deployable Diamond Cut Cold Snare (Micro-Tech Endoscopy, China) with a capture diameter of 10 mm is used. Both instruments are initially positioned in the central working channel of the 6DM. As a target, a 3D-printed polyp (8 mm in diameter) is attached to a deep-seated site within a stomach anatomical model (193 x 30 x 156 mm). Fig. 11 depicts the top view with insets being the camera view. The 6DM is inserted through the

This article has been accepted for publication in IEEE Transactions on Medical Robotics and Bionics. This is the author's version which has not been fully edited and content may change prior to final publication. Citation information: DOI 10.1109/TMRB.2024.3464668

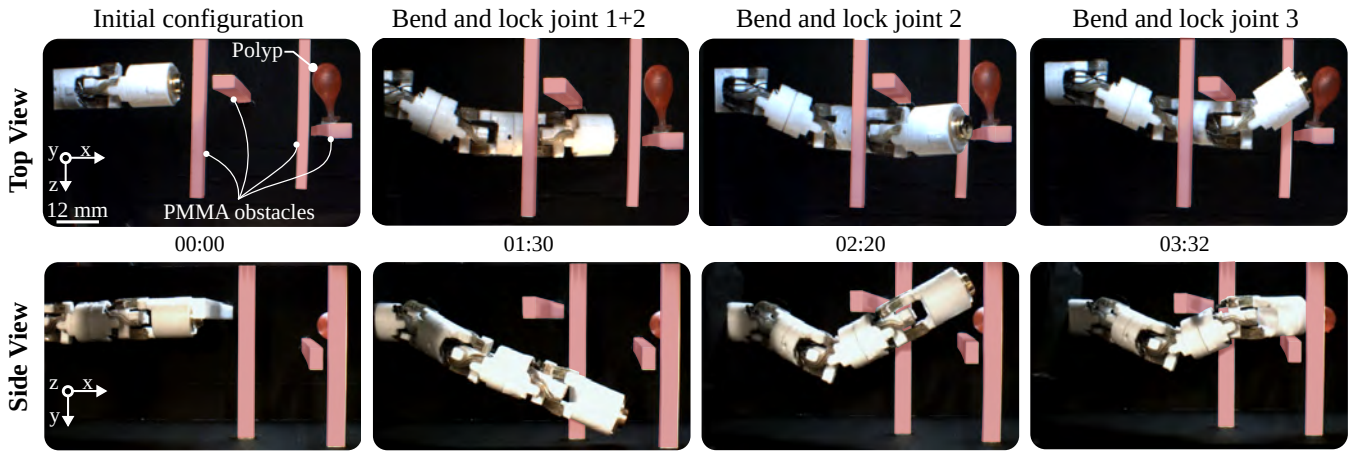

Fig. 10. Demonstration of the manipulator's maneuverability. A container ($10 \times 8 \times 4$ cm) with obstacles made of Polymethyl methacrylate (PMMA) is placed inside the workspace of a Helmholtz coil setup and a red polyp is used as a target. The manipulator can be controlled by the Helmholtz coils to maneuver around the obstacles to reach the target while the insertion is achieved by a linear slide. The top and side views of the manipulators's actions are displayed. The timestamp is given in minutes:seconds.

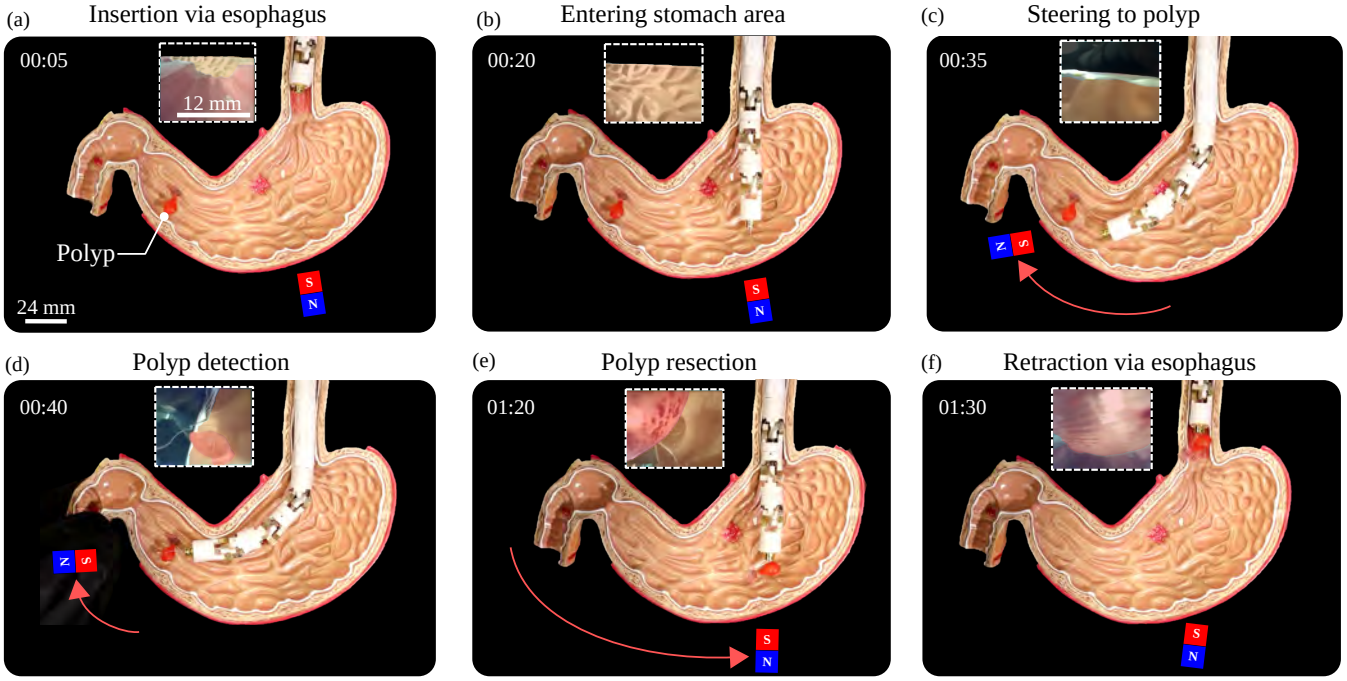

Fig. 11. Simulation of gastroscopy and polypectomy with endoscopic views (insets) and timestamps given in minutes:seconds. (a) Insertion via the esophagus. (b) Entering the stomach using a linear slide. **(c)** Steering to polyp inside stomach phantom using an external permanent magnetic. (d) Polyp detection and inspection via camera followed by shape-locking through passive cooling. (e) Polyp resection using a cold snare. (f) Retraction of polyp via the esophagus.

esophagus (Fig. 11(a)) and advances into the inner stomach area using a linear slide (Fig. 11(b)). Steered by the permanent magnet, the 6DM is deflected in its soft state towards the polyp (Fig. 11(c)). After accessing and inspecting the polyp, all joints are cooled down and the cold snare is deployed through the distal end of the 6DM to remove the polyp (Fig. 11(d)). Finally, The 6DM is heated again and is steered back with the polyp (Fig. 11(e)) and retracted through the esophagus (Fig. 11(f)). The timestamp of each step is shown in the top left corner of Fig. 11(a)-(f). Seven attempts were conducted with an average duration of 1:44 (±18.1) s. Please refer to the supplementary video for the complete demonstration.

IV. Discussion

The proposed U-joint design can be modularly extended to a multi-DOF manipulator, as demonstrated by the 6DM. An overview of the 6DM's specifications can be found in Table III. The U-joint design concentrates 2-DOFs at a single location with intersecting rotation axes leading to a compact design. In contrast, other concepts attain multiple DOFs by arranging 1-DOF joints orthogonally in series, sacrificing compactness [4], [27]. The design employs magnetic actuation, a choice that stands in contrast to tendon- or pneumatic-driven systems. The combination of magnetic actuation and the variable stiffness characteristic of the SMP allows us to control

TABLE III
SPECIFICATIONS OF THE 6-DEGREE-OF-FREEDOM MANIPULATOR

Structure	Specification	Value
6DM	Maximum bending angle range [°]	127
	DOF	6
	Minimum bending radius [mm]	48
	Outer diameter [mm]	12
	Working channel diameter [mm]	2
	Total length [mm]	80
	Weight [g]	6
U-Joint	Maximum bending angle range [°]	42
	Bending stiffness [Nmm/°][(1)]	0.57[(3)] 0.06[(4)]
	Lateral bending stiffness [Nmm/°][(2)]	2.27[(3)] 0.45[(4)]
	Torsional stiffness [Nmm/°]	2.27[(3)] 0.11[(4)]
	Maximum hysteresis [°]	20
Permanent magnet	Outer diameter [mm]	6
	Inner diameter [mm]	2
	Height [mm]	4
	Residual magnetism [T]	1.38
	Magnetic dipole moment [Am^2]	0.114

(1) Bending moment applied along the principal bending plane; (2) Bending moment applied along the lateral bending plane; (3) Stiff state; (4) Soft state.

multiple DOFs using a single permanent magnet, even as more joints are added to the system. This is an advantage over tendon-driven systems [8], [47], where additional DOFs are associated with further routing, cable pulleys, and ultimately friction. Compared to a wire-actuated U-joint [29], our flexure-based design eliminates the need for extra parts like pins and collars, significantly reducing the part count and simplifying manufacture. Unlike pneumatic-driven concepts, our approach eliminates the risk of pinching internal fluidic channels during manipulation.

The proposed U-joint enables a ROM of 60° for each DOF. Shape-locking is essential to maintain this deflection consistently across multiple joints. Thus, each DOF can switch within seconds between a low-stiffness state (0.06 Nmm/°) for accessing a surgical site and a high-stiffness state (0.57 Nmm/°) for securing the 6DM during a surgical task. The selective locking of individual DOFs within a multi-DOF joint or segment is unique compared to other magnetically-actuated designs (Table I). In the current design, the locked DOF provides support stiffness for the unlocked DOF, while in continuum manipulators with bending sections entirely made of SMP, there is no lateral support when heated. Hence, parasitic joint motion is studied as it plays a pivotal role in providing stability against tissue and respiratory motion during operation. In the stiff state, the lateral bending stiffness (perpendicular to the principal bending plane) exceeds the principal bending stiffness by a factor of 4 (2.27 Nmm/° versus 0.57 Nmm/°), and in the rubber phase by a factor of 7.5 (0.45 Nmm/° versus 0.06 Nmm/°). Besides the lateral stiffness, torsional stiffness is crucial to avoid twisting distortions induced by the end-effector. The joint design offers a torsional stiffness of 2.27 Nmm/°. However, when transitioning to the rubber phase, the torsional stiffness diminishes to 0.11 Nmm/°. In response, the joint exhibits an axial elongation, causing the yokes to move apart from each other (see supplementary video). It is noted that the stiffness of the SMP joint is only evaluated experimentally and is not analyzed theoretically.

In the 6DM configuration, it is worth noting that there is an inconsistency in the deflection between joints (Fig 9(a)). This issue arises from the accumulation of torques from the tip to the base, meaning the proximal joints need to support higher loads than the distal joints. Compared to the experimentally determined radius of curvature of 55 mm at 90 ° with one DOF actuated per joint (Fig. 9(b)), the kinematic analysis revealed a theoretical value of 48 mm (Fig. 4). This variance can likely be attributed to manufacturing inaccuracies between joints. Hysteresis can also be observed in Fig. 8(a). It can be attributed to the viscoelastic properties of the SMPs which result in energy dissipation and residual stress during load cycles. Directionally uneven load cycles similarly affect the viscoelastic behavior influencing hysteresis and deflection amplitude. Varying the magnetic actuation method also affects the hysteresis and deflection amplitude. Specifically, a gradual application of magnetic fields (Fig. 8(a)) results in higher deflection amplitudes compared to instantaneously applied fields (Fig. 8(d)). The effects of hysteresis can be compensated by implementing closed-loop control.

The rate of stiffness change is another important parameter for VS devices applied to endoscopic applications, as prolonged medical intervention increases the cost and risk to the patient [48]. By changing the dimensions of the flexible heating element, the heat distribution within the flexure can be fine-tuned. Owing to the large surface-to-volume ratio of the flexure, it can be heated and passively cooled within 14 s and 64 s, respectively. This is an advantage over existing magnetically-actuated designs based on passive cooling (Table I). Implementing an active cooling system could further reduce the cooling and thus the total intervention time. The SMP used in this study reaches its rubber phase at around 60 °C. However, in medical applications, device temperatures must not exceed 41 °C [49]. To prevent heat-induced tissue damage, a coat to thermally insulate the exterior of the 6DM and temperature sensors should be considered. An SMP with a sharper transition temperature could be another option.

Experiments have demonstrated the capability to handle a camera and a cold snare concurrently, both initially placed in the central channel. For procedures requiring frequent insertion and retraction of multiple instruments, silicon tubes must be inserted to create continuous working channels for the surgical tools to slide through. Then, for example, the off-center channels can be used for a water nozzle to purge internal effusion, a light source, additional tools, or active cooling. By integrating the electric circuit into the housing, the cable duct can be used as an additional instrument channel. As shown in section II-B and III-I, the 6DM offers a large workspace and demonstrates enhanced maneuverability. This can reduce the number of entry ports in laparoscopic surgery by replacing multiple rigid instruments. The outer diameter of 12 mm is based on a standard laparoscopic trocar size of 12 mm [15] and on the typical range of 9-15 mm for commercially available

endoscopes used in gastrointestinal tract examinations [3]. The size of the embedded permanent magnet is selected according to the performance of the actuation system used for the mechanical characterization and maneuverability demonstration. With a magnetic dipole moment of $0.114\,\mathrm{Am}^2$, reaching the maximum bending angle requires an external field of 20 mT, well within the expected operational range. The SMP material is selected for its versatile molding possibility and its transition temperature of 35 °C, which requires actuation above body temperature, but not so high as to risk severe injury.

Currently, the system operates on an open control loop, using relatively weak magnetic fields of up to 20 mT. This falls well below the 200 mT safety limit for static and low-frequency ranges ($\leq$1 Hz) recommended by the World Health Organization [50]. By adjusting the volume and dipole moment of the embedded magnet, the field strength required for actuation can be adapted to the actuation system. Hence, the magnetic control is not limited to a specific actuation system, enabling the use of existing commercial systems such as the StereotaxisNiobe (Stereotaxis, USA) and the Aeon Phocus (Aeon Scientific AG, Switzerland) which can generate fields up to 80 mT [28], [51].

V. Conclusions

This work presents a novel design of a VS 2-DOF joint. The design circumvents internal and external space constraints by employing external magnetic actuation and a compact U-joint design. To modulate the joint's stiffness, VS-flexures with custom heating elements embedded between sheets of SMP are used. The flexure-based design reduces the number of parts and simplifies manufacture, demonstrating potential for further miniaturization. The joint design is evaluated for thermal actuation, current-dependent actuation, stiffness against intentional and parasitic motions, and shape-locking. The joint can be modularly extended to form a manipulator, allowing the number of DOFs to be customized and controlled independently with a single permanent magnet. A kinematic analysis is carried out for a 6-DOF version of the manipulator to investigate the theoretical workspace and configuration possibilities. In the experiment, the 6DM avoids obstacles to reach a target location in a confined space. This design opens up new possibilities for accessing and navigating hard-to-reach sites in minimally invasive surgery. To showcase a practical surgical task, a gastroscopy and a polypectomy (*in vitro*) are simulated with commercially available surgical tools that are inserted through the 6DM.

Future work includes the implementation of real-time feedback on shape reconstruction and temperature monitoring to enable closed-loop control. The joint design could benefit from miniaturization for access to smaller workspaces, a reduced cooling time, and strengthening through metals for manufacturing. Additionally, implementing a modular circuit design and integrating custom-designed surgical tools would enhance usability and broaden the field of application.

Acknowledgments

This research has received funding from the Dutch Research Council (NWO) under Grant 19220: Project FlexSmart. The authors would like to thank Prof. Dr. J.P.P.M. de Vries and Dr. R.C.L. Schuurmann for discussions on potential medical applications and insights into robot-assisted surgery.

References

[1] B. S. Peters, P. R. Armijo, C. Krause, S. A. Choudhury, and D. Oleynikov, "Review of emerging surgical robotic technology," *Surgical Endoscopy*, vol. 32, no. 4, pp. 1636–1655, Sep. 2018.

[2] J. J. Craig, "Surgical Robotics: Systems, Applications, and Visions", *Springer New York*, 2010.

[3] D. Song, S. Wang, Z. Zhang, X. Yu, and C. Shi, "A Novel Continuum Overtube with Improved Triangulation for Flexible Robotic Endoscopy," *IEEE Transactions on Medical Robotics and Bionics*, vol. 5, no. 3, pp. 657–668, Aug. 2023.

[4] T. L. Thomas, J. Sikorski, G. K. Ananthasuresh, V. K. Venkiteswaran, and S. Misra, "Design, Sensing, and Control of a Magnetic Compliant Continuum Manipulator," *IEEE Transactions on Medical Robotics and Bionics*, vol. 4, no. 4, pp. 910–921, Nov. 2022.

[5] C. Forbrigger, E. Fredin, and E. Diller, "Evaluating the Feasibility of Magnetic Tools for the Minimum Dynamic Requirements of Microneurosurgery," in *Proc. IEEE International Conference on Robotics and Automation (ICRA)*, 2023, pp. 4703–4709.

[6] Y. Kim, S. S. Cheng, and J. P. Desai, "Active Stiffness Tuning of a Spring-Based Continuum Robot for MRI-Guided Neurosurgery," *IEEE Transactions on Robotics*, vol. 34, no. 1, pp. 1–11, Feb. 2018.

[7] K. Fukushima, T. Kanno, T. Miyazaki, T. Kawase, and K. Kawashima, "Development of selective driving joint forceps using shape memory polymer," in *Proc. IEEE/RSJ International Conference on Intelligent Robots and Systems (IROS)*, 2020, pp. 3125–3130.

[8] T. Kanno, D. Haraguchi, M. Yamamoto, K. Tadano, and K. Kawashima, "A forceps manipulator with flexible 4-DOF mechanism for laparoscopic surgery," *IEEE/ASME Transactions on Mechatronics*, vol. 20, no. 3, pp. 1170–1178, Jun. 2015.

[9] H. Nima, "Stomach Cross Section Anatomy," 3D model (STL), Standard License. [Online]. Available: https://artstn.co/m/bj00r

[10] F. Feng, W. Hong, and L. Xie, "Design of 3D-Printed Flexible Joints with Presettable Stiffness for Surgical Robots," *IEEE Access*, vol. 8, pp. 79 573–79 585, 2020.

[11] W. Hong, L. Xie, J. Liu, Y. Sun, K. Li, and H. Wang, "Development of a Novel Continuum Robotic System for Maxillary Sinus Surgery," *IEEE/ASME Transactions on Mechatronics*, vol. 23, no. 3, pp. 1226–1237, Jun. 2018.

[12] Y. J. Kim, S. Cheng, S. Kim, and K. Iagnemma, "A stiffness-adjustable hyperredundant manipulator using a variable neutral-line mechanism for minimally invasive surgery," *IEEE Transactions on Robotics*, vol. 30, no. 2, pp. 382–395, Apr. 2014.

[13] T. Ranzani, M. Cianchetti, G. Gerboni, I. D. Falco, and A. Menciassi, "A Soft Modular Manipulator for Minimally Invasive Surgery: Design and Characterization of a Single Module," *IEEE Transactions on Robotics*, vol. 32, no. 1, pp. 187–200, Feb. 2016.

[14] H. M. Le, T. N. Do, and S. J. Phee, "A survey on actuators-driven surgical robots," *Sensors and Actuators, A: Physical*, vol. 247, pp. 323–354, Aug. 2016.

[15] D. Haraguchi, T. Kanno, K. Tadano, and K. Kawashima, "A Pneumatically Driven Surgical Manipulator with a Flexible Distal Joint Capable of Force Sensing," *IEEE/ASME Transactions on Mechatronics*, vol. 20, no. 6, pp. 2950–2961, Dec. 2015.

[16] B. Zhang, C. Hu, P. Yang, Z. Liao, and H. Liao, "Design and Modularization of Multi-DoF Soft Robotic Actuators," *IEEE Robotics and Automation Letters*, vol. 4, no. 3, pp. 2645–2652, Jul. 2019.

[17] M. Richter, V. K. Venkiteswaran, and S. Misra, "Multi-Point Orientation Control of Discretely-Magnetized Continuum Manipulators," *IEEE Robotics and Automation Letters*, vol. 6, no. 2, pp. 3607–3614, Apr. 2021.

[18] M. P. Kummer, J. J. Abbott, B. E. Kratochvil, R. Borer, A. Sengul, and B. J. Nelson, "OctoMag: An electromagnetic system for 5-DOF wireless micromanipulation," in *Proc. IEEE International Conference on Robotics and Automation*, 2010, pp. 1610–1616.

[19] J. Sikorski, I. Dawson, A. Denasi, E. E. G. Hekman, and S. Misra, "Introducing BigMag- A novel system for 3D magnetic actuation of flexible surgical manipulators," in *Proc. IEEE International Conference on Robotics and Automation (ICRA)*, 2017, pp. 3594–3599.

[20] J. Edelmann, A. J. Petruska, and B. J. Nelson, "Magnetic control of continuum devices," *The International Journal of Robotics Research*, vol. 36, no. 1, pp. 68–85, 2017.

[21] D. Chathuranga, P. Lloyd, J. H. Chandler, R. A. Harris, and P. Valdastri, "Assisted Magnetic Soft Continuum Robot Navigation via Rotating Magnetic Fields," *IEEE Robotics and Automation Letters*, vol. 9, no. 1, pp. 183–190, Jan. 2024.

[22] A. Hong, A. J. Petruska, A. Zemmar, and B. J. Nelson, "Magnetic Control of a Flexible Needle in Neurosurgery," *IEEE Transactions on Biomedical Engineering*, vol. 68, no. 2, pp. 616–627, Feb. 2021.

[23] A. Lim, A. Schonewille, C. Forbrigger, T. Looi, J. Drake, and E. Diller, "Design and Comparison of Magnetically-Actuated Dexterous Forceps Instruments for Neuroendoscopy," *IEEE Transactions on Biomedical Engineering*, vol. 68, no. 3, pp. 846–856, Mar. 2021.

[24] G. Pittiglio, M. Mencattelli, and P. E. Dupont, "Magnetic Ball Chain Robots for Endoluminal Interventions," in *Proc. IEEE International Conference on Robotics and Automation (ICRA)*, 2023, pp. 4717–4723.

[25] Y. J. Kim, S. Cheng, S. Kim, and K. Iagnemma, "A novel layer jamming mechanism with tunable stiffness capability for minimally invasive surgery," *IEEE Transactions on Robotics*, vol. 29, no. 4, pp. 1031–1042, 2013.

[26] M. Brancadoro, M. Manti, F. Grani, S. Tognarelli, A. Menciassi, and M. Cianchetti, "Toward a variable stiffness surgical manipulator based on fiber jamming transition," *Frontiers Robotics AI*, vol. 6, 2019.

[27] H. C. Wang, S. H. Cui, Y. Wang, and C. L. Song, "A hybrid electromagnetic and tendon-driven actuator for minimally invasive surgery," *Actuators*, vol. 9, no. 3, Sep. 2020.

[28] C. Chautems, A. Tonazzini, D. Floreano, and B. J. Nelson, "A Variable Stiffness Catheter Controlled with an External Magnetic Field," in *Proc. IEEE/RSJ International Conference on Intelligent Robots and Systems (IROS)*, 2017, pp. 181–186.

[29] L. Manfredi and A. Cuschieri, "Design of a 2 DOFs mini hollow joint actuated with SMA wires," *Materials*, vol. 11, no. 10, Oct. 2018.

[30] T. L. Thomas, J. Bos, J. J. Huaroto, V. Kalpathy Venkiteswaran, and S. Misra, "A Magnetically Actuated Variable Stiffness Manipulator Based on Deployable Shape Memory Polymer Springs," *Advanced Intelligent Systems*, vol. 6, no. 2, 2024, Art. no. 2200465.

[31] J. Lussi, M. Mattmann, S. Sevim, F. Grigis, C. De Marco, C. Chautems, S. Pané, J. Puigmartí-Luis, Q. Boehler, and B. J. Nelson, "A Submillimeter Continuous Variable Stiffness Catheter for Compliance Control," *Advanced Science*, vol. 8, no. 18, Sep. 2021, Art. no. 2101290.

[32] C. Chautems, A. Tonazzini, Q. Boehler, S. H. Jeong, D. Floreano, and B. J. Nelson, "Magnetic Continuum Device with Variable Stiffness for Minimally Invasive Surgery," *Advanced Intelligent Systems*, vol. 2, no. 6, Jun. 2020, Art. no. 1900086.

[33] A. J. Taylor, T. Slutzky, L. Feuerman, H. Ren, J. Tokuda, K. Nilsson, and Z. T. H. Tse, "MR-Conditional SMA-Based Origami Joint," *IEEE/ASME Transactions on Mechatronics*, vol. 24, no. 2, pp. 883–888, Apr. 2019.

[34] G. Ehrmann and A. Ehrmann, "3D printing of shape memory polymers," *Journal of Applied Polymer Science*, vol. 138, no. 34, Sep. 2021, Art. no. 50847.

[35] G. Scalet, "Two-way and multiple-way shape memory polymers for soft robotics: An overview," *Actuators*, vol. 9, no. 1, Mar. 2020.

[36] Y. Piskarev, J. Shintake, C. Chautems, J. Lussi, Q. Boehler, B. J. Nelson, and D. Floreano, "A Variable Stiffness Magnetic Catheter Made of a Conductive Phase-Change Polymer for Minimally Invasive Surgery," *Advanced Functional Materials*, vol. 32, no. 20, May 2022, Art. no. 2107662.

[37] Y. Piskarev, Y. Sun, M. Righi, Q. Boehler, C. Chautems, C. Fischer, B. J. Nelson, J. Shintake, and D. Floreano, "Fast-Response Variable-Stiffness Magnetic Catheters for Minimally Invasive Surgery," *Advanced Science*, 2024, Art. no. 2305537.

[38] M. Mattmann, Q. Boehler, X.-Z. Chen, S. Pané, and B. J. Nelson, "Shape memory polymer variable stiffness magnetic catheters with hybrid stiffness control," in *Proc. IEEE/RSJ International Conference on Intelligent Robots and Systems (IROS)*, 2022, pp. 9589–9595.

[39] A. Firouzeh, S. Mirrazavi, A. Billard, and J. Paik, "An under actuated robotic arm with adjustable stiffness shape memory polymer joints," in *Proc. IEEE International Conference on Robotics and Automation*, 2015, pp. 2536–2543.

[40] A. Firouzeh and J. Paik, "Grasp Mode and Compliance Control of an Underactuated Origami Gripper Using Adjustable Stiffness Joints," *IEEE/ASME Transactions on Mechatronics*, vol. 22, no. 5, pp. 2165–2173, 2017.

[41] H. Huang, E. Dong, M. Xu, J. Yang, and K. H. Low, "Mechanism design and kinematic analysis of a robotic manipulator driven by joints with two degrees of freedom (DOF)," *Industrial Robot*, vol. 45, no. 1, pp. 34–43, Jan. 2018.

[42] E. Tank and V. Parlaktaş, "Compliant cardan universal joint," *Journal of Mechanical Design*, vol. 134, no. 2, 2012.

[43] J. J. Craig, "Introduction to Robotics Mechanics and Control.", *Pearson*, 3. Edition, 2005.

[44] Y. Meng, J. Jiang, and M. Anthamatten, "Body temperature triggered shape-memory polymers with high elastic energy storage capacity," *Journal of Polymer Science, Part B: Polymer Physics*, vol. 54, no. 14, pp. 1397–1404, Jul. 2016.

[45] W. Small IV, P. Singhal, T. S. Wilson, and D. J. Maitland, "Biomedical applications of thermally activated shape memory polymers," *Journal of Materials Chemistry*, vol. 20, no. 17, pp. 3356–3366, Mar. 2010.

[46] H. Goldman and D. A. Antonioli, "Mucosal biopsy of the esophagus, stomach, and proximal duodenum." *Hum Pathol.*, vol. 13, no. 5, pp. 423–48, May 1982.

[47] X. Ma, X. Wang, Z. Zhang, P. Zhu, S. S. Cheng, and K. W. S. Au, "Design and Experimental Validation of a Novel Hybrid Continuum Robot With Enhanced Dexterity and Manipulability in Confined Space," *IEEE/ASME Transactions on Mechatronics*, vol. 28, no. 4, pp. 1826–1835, Aug. 2023.

[48] L. Blanc, A. Delchambre, and P. Lambert, "Flexible medical devices: Review of controllable stiffness solutions," *Actuators*, vol. 6, no. 3, Sep. 2017.

[49] Y. Haga, T. Mineta, T. Matsunaga, and N. Tsuruoka, "Micro-Robotic Medical Tools Employing SMA Actuators for Use in the Human Body," pp. 1233–1244, Dec. 2022.

[50] International Commission on Non-Ionizing Radiation Protection., "Guidelines for limiting exposure to time-varying electric, magnetic and electromagnetic fields (up to 300 GHz)," *Health Physics*, pp. 494–522, 1998.

[51] F. Carpi and C. Pappone, "Stereotaxis Niobe magnetic navigation system for endocardial catheter ablation and gastrointestinal capsule endoscopy," *Expert Review of Medical Devices*, vol. 6, no. 5, pp. 487–498, Sep. 2009.